JOURNAL OF MATERIALS RESEARCH AND TECHNOLOGY 2022;17:3246–3261

Available online at www.sciencedirect.com

jmr&t
Journal of Materials Research and Technology

journal homepage: www.elsevier.com/locate/jmrt

Original Article

# Carbon nanofiber-polyelectrolyte triggered piezoelectric polymer-based hydrophilic nanocomposite for high sensing voltage generation

*Lokesh Singh Panwar* [a], *Varij Panwar* [a,**], *Gopinathan Anoop* [b], *Sukho Park* [c,*]

[a] *Department of Electronics and Communication Engineering, Graphic Era (Deemed to be University), Dehradun, India*
[b] *School of Materials Science and Engineering, Gwangju Institute of Science and Technology, Oryong-Dong, Buk-Gu, Gwangju, 61005, South Korea*
[c] *Department of Robotics Engineering, Daegu Gyeongbuk Institute of Science and Technology (DGIST), Daegu, South Korea*

## ARTICLE INFO

*Article history:*
Received 18 December 2021
Accepted 15 February 2022
Available online 24 February 2022

*Keywords:*
PVDF
PAMPS
Nanorods
Pressure sensor
Flexibility
Piezoelectric
Nanocomposite

## ABSTRACT

Flexible electronic devices with flexible sensors have drawn enormous attention due to their wide variety of applications, such as wearable health monitoring devices, bendable touch screens, flexible storage devices, artificial skins, etc. However, the mechanical and electrical performance of devices should be enhanced by new materials design or an innovative device structure to fulfill the requirements for such applications. Here, a poly(vinylidenefluoride) (PVDF) piezoelectric polymer-based hydrophilic nanocomposite (PHNC) sensing membrane using carbon nanofibers (CNF) and poly-acrylamido-methyl-propane-sulfonic acid (PAMPS) polyelectrolyte exhibiting enhanced mechanical and electrical performance is demonstrated. The hydrophilic PAMPS intruded in the PVDF/CNF composition, triggering microstructural changes and facilitating a strong polar β-phase PVDF formation. A dc conductivity of 0.43 S/cm and high electric current density (3.64 μA/cm$^2$) were achieved from PVDF/CNF/PAMPS (80/2/18) PHNC. The piezoelectric performance of the PHNC was investigated for several bending cycles, and it generates the maximum peak output voltage up to 3.65 V under the repeated bending-releasing test procedure. A wearable sensor application is demonstrated by exposing it to different human body movements. During finger motion and elbow movements, the developed PHNC generated piezoelectric maximum peak output voltage up to 3.58 V at a bending angle of 180° for finger motion and 2.2 V for elbow movement. The fabricated PHNC are highly flexible and exhibit outstanding reproducibility and reliability, making them ideal for energy harvesting, the self-powered sensor in wearable electronic devices, electronic skin (e-skin), and soft robotics applications.

---

** Corresponding author.,
* Corresponding author.

E-mail addresses: varijpanwarcertain@gmail.com (V. Panwar), shpark12@dgist.ac.kr (S. Park).

https://doi.org/10.1016/j.jmrt.2022.02.075

## 1. Introduction

The rapid development of artificial intelligence (AI) and the internet of things (IoT) emphasize the fabrication of wearable, foldable, portable, and stretchable smart devices for human-machine interaction applications. The highly efficient, flexible, and wearable pressure sensors are the most significant electronic device for human motion monitoring and human-machine interface implementation in signal collection [1–8]. Various pressure sensors have already been described, including piezocapacitive, piezoresistive, and piezoelectric sensors [9–11]. However, for real-time sensing applications, it is necessary to have not only the capacity to convert mechanical stimuli to electrical signals but also the capacity to respond quickly and linearly along with good signal stability [12], both of which are difficult to achieve with piezoresistive and piezocapacitive pressure sensors [13–15]. Furthermore, employing renewable energy sources to power such devices is critical for energy and environmental sustainability. The piezoelectric materials are a special type of materials; when they are mechanically stimulated, they deform and change polarization density immediately, electrical voltage induces in the polar direction [16,17]. As a result, the mechanical parameters of piezoelectric polymer material are crucial in improving their piezoelectricity and ensuring adequate stress distribution during mechanical compression, which is generally overlooked. Although several studies have focused on the piezoelectric sensing performance of polymers and the influence of Young's modulus on the piezoelectric capabilities of polymers, mechanical parameters such as flexibility and tensile strength require further consideration [18–20].

Organic piezoelectric materials have focused much interest in developing flexible and wearable electronics devices for pressure sensing applications because of their flexibility, greater biocompatibility, lower density, lightweight, and ease of processing than inorganic piezoelectric materials [10]. Because of its high piezoelectric coefficient, polyvinylidene fluoride (PVDF) is the most extensively utilized organic piezoelectric material. However, their piezoelectric coefficient is substantially lower when compared to piezoelectric ceramics, hindering itself-powered sensor operation [21]. PVDF is a semi-crystalline fluoro-polymer made from $H_2C{=}CF_2$ monomer after polymerization; it has five crystalline phases, namely $\alpha$, $\beta$, $\gamma$, $\delta$ and$\varepsilon$, because of the antiparallel orientation of the dipoles, the $\alpha$, and $\varepsilon$ phases are non-polar. The $\alpha$-phase is the most stable, and it has TGTG' (trans-gauche-trans-gauche) conformation. Due to its all-trans chain structure (TTTT), the dipole moments of the $\beta$-phase PVDF are the highest and show excellent piezoelectric and ferroelectric capabilities of all the polymorphs [22,23]. Thus, the $\beta$-phase PVDF has grabbed the attention of many researchers in its development and technological applications.

The $\beta$-phase PVDF can be obtained by two important methods–(i) mechanical stretching and (ii) interfacial interactions. The $\alpha$-phase PVDF formed by mechanically stretching the melt or blend can be directly converted to $\beta$-phase PVDF; however, achieving high content $\beta$-phase of PVDF crystal through traditional melt and solution processing is typically difficult [22,24,25]. Another method for developing $\beta$-PVDF is to develop a nanocomposite by investigating intermolecular interactions between PVDF matrix and nanofillers. There are several studies on the fabrication of PVDF nanocomposites due to the wide variety of nanofillers and the ease of mixing. In general, nanofillers are divided into two types–inorganic and organic. Various inorganic nanofillers have been explored to improve the polar $\beta$-phase contents in PVDF, for example, $BaTiO_3$ [26–28], ZnO [29,30], aluminium oxide [31], silver nanowires (AgNWs) [32,33]. The PVDF-nanocomposite using these inorganic nanofillers has high $\beta$-phase content, while these nanocomposites are brittle and fragile. Thus, these are not suitable for wearable and flexible devices.

As a result of excellent solution processability, non-toxic and low-cost qualities, biodegradability, and good ferroelectric capabilities, organic nanofillers have attracted extensive interest, for example, graphene oxide (GO) [34] and reduced-graphene-oxide (rGO) [35,36]. Rahman et al. [37] discovered that PVDF/rGO flexible piezoelectric nanocomposite film has a higher peak–peak sensing voltage (1.3 V) than PVDF/GO piezoelectric nanocomposite film (0.9 V) and pure PVDF piezoelectric film (0.7 V) due to the enhanced polarization by adding reduced-graphene-oxide (rGO) in the PVDF. Yu et al. [38] found that when CNT is added to PVDF, the piezoelectric ability of the fibrous, flexible PVDF membrane was greatly enhanced due to higher surface density and the higher nucleation effect of carbon nanotube (CNT) for the $\beta$-phase of PVDF. However, due to inadequate interfacial interaction between typical conductive fillers and PVDF molecular chains, achieving a strong filler–dipole interface and improving the dipole polarization of piezoelectric PVDF is challenging. The CNF is another carbon-based nanofiller to induce the $\beta$- PVDF by forming a PVDF nanocomposite because CNF has superior electrical conductivity, thermal stability, as well as high mechanical strength [39,40]. Because of its promising applications in electrostatic dissipation, the electrical conductivity of a PVDF with carbon-based nanofiller has attracted research interest. However, the insufficient dispersion of CNF in the PVDF matrix challenges their use as nanofiller to form PVDF nanocomposites. With the help of a chemical modification, the dispersion of CNF in the PVDF matrix has been enhanced [23,41].

In the present research, polyelectrolyte poly(2-acrylamido-2-methyl-1-propanesulfonic acid) PAMPS is used to perform chemical modification for homogenous dispersion of CNF in the PVDF matrix. PAMPS has a strong anionic polyelectrolyte property and good water permeability owing to the presence of a hydrophilic sulfonic acid group [$S({=}O)_2{-}OH$]. Sulfonic groups are hydrophilic, which increases water sorption rather than organic chemical sorption, desirable for chemical protective membranes [42]. Following that, the CNF/PAMPS is blended with the PVDF matrix using the solution casting process (see Fig. 1(a)) to fabricate the PVDF/CNF/PAMPS PHNC rendering the CNF/PAMPS homogeneously dispersed in the throughout PVDF matrix. This occurs when the sulfonic acid groups of PAMPS are bound to the CNF. Interfacial interactions between the CNF and the polymer matrix can also form continuous proton transfer paths, indicating that the sulfonic acid groups were evenly distributed on the surface of the PVDF/CNF/PAMPS PHNC for proton exchange (see in Fig. 1(b)).

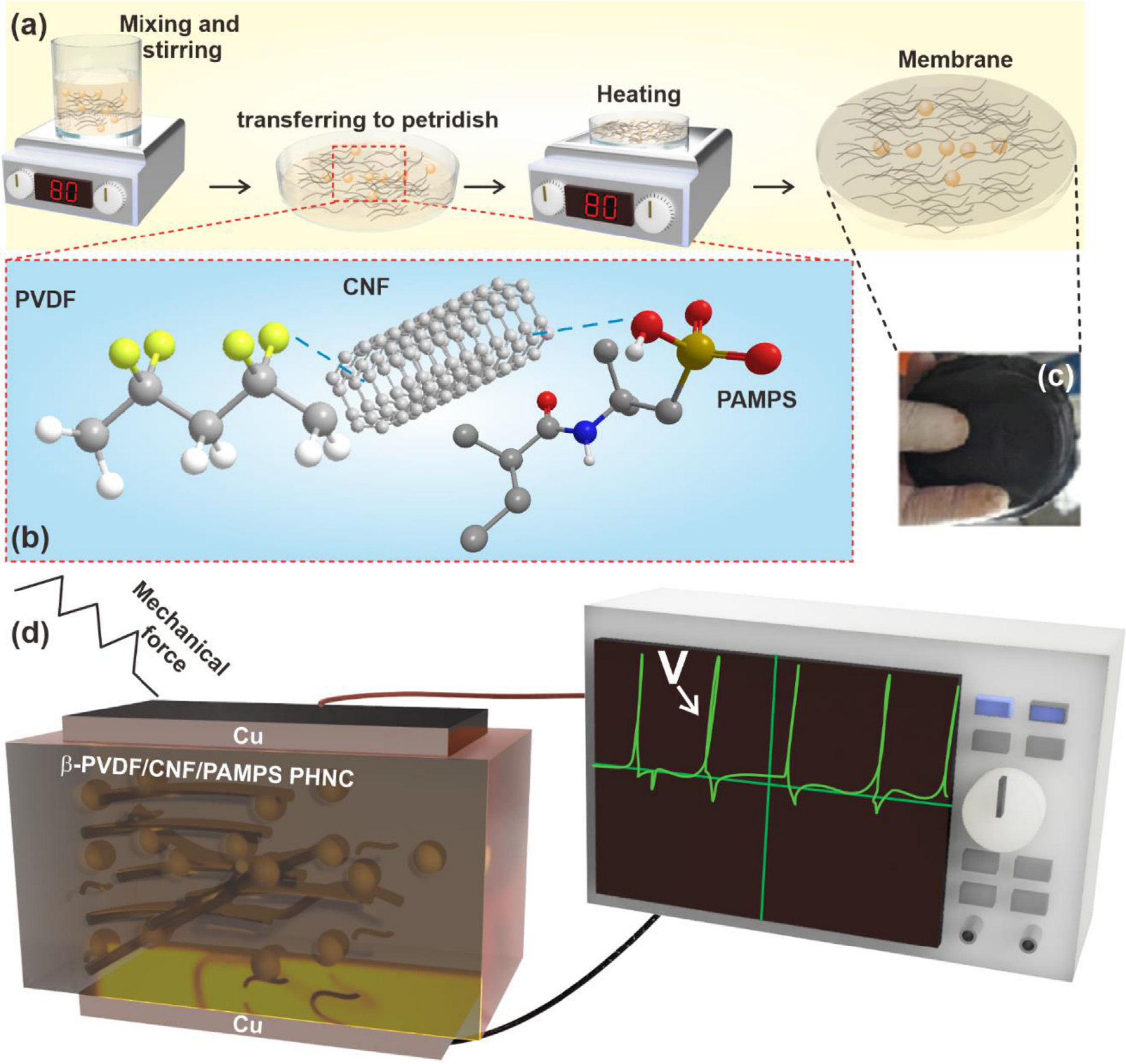

**Fig. 1 – (a) Preparation process, (b) Structural characterization, (c) Optical image of the PVDF/CNF/PAMPS PHNC, and (d) Schematic diagram of the β-phase PVDF/CNF/PAMPS PHNC based sensor with the generation of voltage signal with bending strain.**

This behavior is likely because CNF and PAMPS have relatively strong hydrogen bond interactions. With an increase in the concentration of PAMPS, numbers of sulphonic groups are attached to the carbon network, increasing the surface bonding and charge flow through the CNF conductive nanorods throughout the PVDF matrix. Therefore, the β-phase improves in PVDF/CNF/PAMPS PHNC. Figure 1(b) shows the chemical structure of PVDF/CNF/PAMPS PHNC. Figure 1(c) shows the optical image of PVDF/CNF/PAMPS PHNC. Figure 1(d) shows a schematic diagram of the β-phase PVDF/CNF/PAMPS PHNC based sensor with the voltage signal generation with bending strain. The FTIR, XRD, and DSC results were utilized to investigate the enhancement of polar β-phase in PHNC. Furthermore, the piezoelectric response of the PHNCs is examined by exposing it to various environments such as bending machine vibrations with adequate bending cycles and human body motions during finger motion and elbow movements.

## 2. Materials and methods

### 2.1. *Materials*

PVDF was obtained from Sigma Aldrich under brand number 182702, with an average molecular weight (Mw) of 534,000 g/mol and a density of 1.74 g/ml at 25 °C. Graphitized (iron-free) Carbon nanofiber (CNF) has also been procured from Sigma Aldrich (trade name 719,781) with 130 nm average diameter, 20 μm fiber length, and 1.90 g/ml density at 25 °C. PAMPS solution (poly(2-acrylamido-2-methyl-1-propanesulfonic acid)) was also bought from Sigma Aldrich under the product name 191,973-100G, with an average molecular weight of 2,000,000 and a concentration of 15% in $H_2O$. The solvent N, N-dimethylformamide (DMF) was obtained from Sigma Aldrich under brand number 57457 and used to dissolve the PVDF, CNF, PAMPS mixture and form a homogeneous solution. Sigma

Aldrich has provided ethanol, an anti-solvent used to neutralize the residual solvent.

### 2.2. Synthesis of PHNCs

The PHNC films were fabricated using a solution casting method shown in Fig. 1(a). To prepare the PHNC film, the different solute components (PVDF, CNF, and PAMPS) were dissolved in DMF. A 100 wt% homogeneous solution was made by combining the weight of 10% solute with 90% solvent to make the final solution. The final whole mixture was dissolved in the homogeneous solution at ~80 °C on a hotplate with a magnetic stir at 450 rpm for 6 h; then the blended solution was poured into a petri dish and again heated at ~80 °C for 10 h until the solvent was completely evaporated from the PHNC film. Once the solvent was completely evaporated, the Petri dish was left at room temperature for cooling. Lastly, the PHNC film on the petri dish was tripped off. The dried film was immersed in 95% technical grade ethanol, an anti-solvent for DMF, for 24 h at 60 °C to remove residual solvent. A series of PVDF/CNF/PAMPS PHNC films were produced under identical conditions. Four different PHNC films were fabricated using different weight ratios (w/w/w, PVDF/CNF/PAMPS), as follows: (98/2/0), (90/2/8), (80/2/18), and (70/2/28).

### 2.3. Characterization

#### 2.3.1. Morphological analysis

The morphological investigation (microstructure characterization) of the fabricated PHNC membrane was performed using a field emission-scanning electron microscope (FE-SEM). In FE-SEM, surface and cross-section images were acquired using a secondary electron detector at a 15 keV acceleration voltage. The FE-SEM machine (MIRA3b TESCAN, USA) was used to examine the surface morphologies and microstructures of fractured PHNC films. An energy dispersive spectroscopy (EDS) analysis was performed to confirm the chemical formation of nanocomposite films. EDS is a chemical technique employed in conjunction with SEM used to identify the contents of each material presented in the proposed membrane.

#### 2.3.2. Crystallization analysis

The crystallization behavior of the sample membranes was examined using an X-ray diffractometer (XRD, Rigaku Ultima IV, Japan) with Cu Kα radiation ($\lambda = 0.1541$ nm). The tests were conducted at 40 kilo-Volt and 40 mA with a scanning rate of 2° $\text{min}^{-1}$ throughout the angle range $2\theta = 5° - 90°$. The degree of crystallinity of PHNC is calculated by the following formula.

$$\textit{Crystallinity of PHNC} = \frac{\textit{Area of crystalline peaks in XRD patterns}}{\textit{Area of all peaks in XRD pattern}} \tag{1}$$

#### 2.3.3. FTIR analysis (chemical characterization)

The chemical composition of the nanocomposite membranes was identified by Fourier Transforms Infrared Spectroscopy (FT-IR, PerkinElmer L160000V) set at the following parameters (ranges 400-4000 $\text{cm}^{-1}$, resolution 4 $\text{cm}^{-1}$, and diaphragm diameter 1 cm). The formula is used to calculate the percentage fraction of β-phase F(β) in the PHNC.

$$F(\beta)(\%) = \frac{A_\beta}{\left(\frac{K_\beta}{K_\alpha}\right)A_\alpha + A_\beta} \times 100 \tag{2}$$

where, $A_\alpha$ and $A_\beta$ are the absorbance value obtained at 764 $\text{cm}^{-1}$ and 840 $\text{cm}^{-1}$, respectively. The $K_\alpha = 6.1 \times 10^4$ and $K_\beta = 7.7 \times 10^4$ are absorbance coefficient at 764 $\text{cm}^{-1}$ and 840 $\text{cm}^{-1}$ respectively.

#### 2.3.4. Thermal analysis

Differential Scanning Calorimetry (DSC, EXSTAR Model-SII 6300 EXSTAR) is a thermal analysis method for PHNC films that examines the thermal behavior of fabricated PHNC membranes using approx. 15 mg samples. The DSC analysis of PHNC was performed under nitrogen ambient with a flow rate of 200 ml/min and a heating rate of 10 °C/min. The crystallinity ($X_c$) of the PHNC sample membrane using DSC thermograph may be determined by equation (3):

$$X_c(\%) = \frac{\Delta H_m}{\Delta H^*_m} \times 100 \tag{3}$$

where $\Delta H_m$ is the melting enthalpy of the PHNC samples obtained from the second melting curve, $\Delta H^*_m$ presents the melting enthalpy when the crystallinity of the polymer is 100%, $\Delta H^*_m$ of PVDF mentioned in the literature are 104.5 J/g.

#### 2.3.5. Mechanical analysis

The universal tensile testing equipment (Instron-3366) was used to assess mechanical characteristics; tensile strength, flexibility, Young's modulus, stiffness, durability, and tensile strain of PHNC membranes. The mechanical behavior was investigated using a tensile test with a 10 mm/min stretching rate and a bending test with 5 mm/min at a 10 mm bending radius. The bending strain ($\varepsilon^b$) was evaluated by equation (4), where $t$ symbolizes the thickness of the PHNC membrane and $r$ signifies the bending radius of the membrane strip.

$$\varepsilon^b = \frac{t}{2r} \tag{4}$$

The bending strain was calculated to be 0.009.

#### 2.3.6. Electrical analysis

The electrical behavior of PHNC films was investigated at room temperature by E4900A-impedance analyzer (Keysight Technologies, Germany), operating at 20 Hz to 1 MHz frequency band, and Teflon-coated stainless steel parallel plate probes (16451B) were used to collect the data from it. The value of capacitances and dielectric loss factor (*tan δ*) of films were a function of frequency and acquired directly from the impedance analyzer, and dielectric constants ($\varepsilon$) were computed using the following relationship:

$$\varepsilon = \frac{C \times t}{\varepsilon_0 \times A} \tag{5}$$

where $C$, $t$ and $A$ denotes the capacitance, thickness and cross-sectional area of the PHNC membrane, $\varepsilon_0$ represents the permittivity of vacuum (free space), the typical value $\varepsilon_0$ is $8.854 \times 10^{-12}$ F/m. Further, the conductivity ($\sigma_{ac}$) was calculated using equation (6) with angular frequency $\omega = 2\pi f$ rad/sec, here, $f$ signifies the operating frequency in Hz,

$$\sigma_{ac} = \omega\, \varepsilon_0\, \varepsilon \tan\delta \tag{6}$$

The dc conductivity (S/cm) of the PHNC membrane was obtained using equation (7), as follows:

$$\sigma_{dc} = \frac{t}{R \times A} \tag{7}$$

where $\sigma_{dc}$ is proton conductivity, t symbolizes the thickness of the PHNC membrane, and R is the resistance evaluated from a complex impedance (Z*) or Nyquist plot of the real impedance (Z′) axis versus the imaginary impedance (Z″) axis, and surface area of membrane is denoted by A.

### 2.3.7. *Water uptake (WUP)*

The electrochemical analysis involved in the experiment includes water uptake and contact angle test. The results provide the hydrolytic property of the piezoelectric polymer-based hydrophilic nanocomposite (PHNC) membrane. Before measuring water uptake, the sample was placed in a vacuum oven at 80 °C for 12 h to remove any retained moisture. The weight of the dry PHNC membrane was then measured and compared to the variations in water sorption over a 24-h immersion period. Water uptake (WUP) is calculated as the difference between the weights of the dried and fully wet membranes using equation (8):

$$WUP = \frac{(W_{wet} - W_{dry})}{W_{dry}} \tag{8}$$

where $W_{wet}$ and $W_{dry}$ are the weights of the wet and dried PHNC membranes, respectively.

### 2.3.8. *Contact angle test*

The Contact angle of the PHNC membrane surface is measured by dropping a deionized water droplet over the membrane surface and measured using a drop shape analyzer (KRUSS-DSA25E). The value below 90° of the contact angle represents the hydrophilic behavior of the membrane. Hydrophilicity refers to a membrane's tendency to allow liquid to pass through its pores.

### 2.3.9. *Sensing measurement*

By applying certain pressure or mechanical bending to the PVDF/CNF/PAMPS piezoelectric polymer-based- hydrophilic nanocomposite (PHNC) films, generates voltage, measured by a Digital Storage Oscilloscope (DSO, Keysight-DSO1052B). The experimental setup for measuring a piezoelectric output voltage from PHNC membranes is shown in Fig. S1, including the DSO, bending machine, and control panel. In this setup, the film is placed between the two electrode terminals of the bending machine. Both electrodes are connected to the output terminal of the control panel, to which DSO's probe was externally connected. This DSO shows the sensing voltage generated by the PHNC film. When moving a rotating knob on the panel, the membrane attached between electrodes was bent, generating an output voltage.

### 2.3.10. *Cyclic current -voltage (CV) characterization*

The cyclic spectrum of the current density and voltage of the PHNC membrane were evaluated using Cyclic-Voltammeter (Metrohm Autolab; PGSTAT204). The cyclic voltammetry (CV) test is performed by applying a positive (charging) voltage sweep $dV/dt$ (scan rate) in a specific voltage range and then immediately reversing (discharging) the voltage sweep polarity after the maximum voltage is reached. Using CV, the electrochemical behavior of a LiCl-dipped PVDF/CNF/PAMPSPHNC membrane was investigated. The cyclic current–voltage graph was also used to calculate the capacitance of the PHNC membrane using the following equation,

$$C = \frac{|i_1 - i_2|/2}{dV/dt} \tag{9}$$

where ΔI denotes total current ($|i_1 - i_2|$) and $dV/dt$ is the voltage scan rate (V/s) of the CV curve.

## 3. Results and discussion

### 3.1. *SEM analysis of PHNCs*

The surface and cross-sections SEM images of various compositions of the PHNCs were carried out to study the morphological (microstructure) analysis of PHNC. The pure PVDF film has a very smooth and clean surface with no impurities or porosity [43]. The surface images of the PVDF/CNF (98/2) and PVDF/CNF/PAMPS (80/2/18) PHNC are shown in Fig. S2(a) and Fig. S2(b), respectively. Fig. S2(a) reveals randomly oriented CNFs in the shapes of nanorods dispersed with smooth and uniform PVDF surfaces; the surface morphology grew more packed and interconnected in this picture, and the CNF Nanorods were confined within the porous structure of PVDF. The SEM images of the PVDF/CNF/PAMPS (80/2/18) PHNC are shown in Fig. S2(b). The PVDF/CNF/PAMPS (80/2/18) PHNC has a layer of mulch on the surface, indicating that PAMPS has been grafted into the membrane. The grafting of PAMPS on the surface of the CNF nanorods causes some agglomeration for membranes containing PAMPS nanoparticles.

The cross-sectional SEM image of pure PVDF shows the spherulitic structure that reflects the semi-crystalline α-phase PVDF as reported in prior studies [43]. Figure 2(a)-(b) show the cross-sectional SEM images of the PVDF/CNF (98/2) PHNC with a magnification of 5kX and 40kX, respectively. From these images, it was observed that the CNF in the shape of nanorods submerged in the PVDF polymeric matrix and well-interconnected to create a conductive composite material, which is responsible for increasing the conductivity of the nanocomposites membrane. The white arrow shows the CNF nanorods. With the addition of CNF content in the PVDF matrix, spherulites are not formed (as observed in Fig. 2(a)), which indicates that the blending of CNF with PVDF triggers the formation of β-phase PVDF. The CNF served as conductive channels and a binding agent to improve the mechanical characteristics of the PHNCs. In addition to that, the spherulitic crystalline structures in the PVDF matrix are transformed into microfibrillar crystals found in SEM images of PVDF/CNF (98/2) PHNC. The change from α-to β crystal PVDF is aided by such crystal structural alignment. As a result, the CNF is in charge of improving stiffness and conductivity sample 98/2/0.

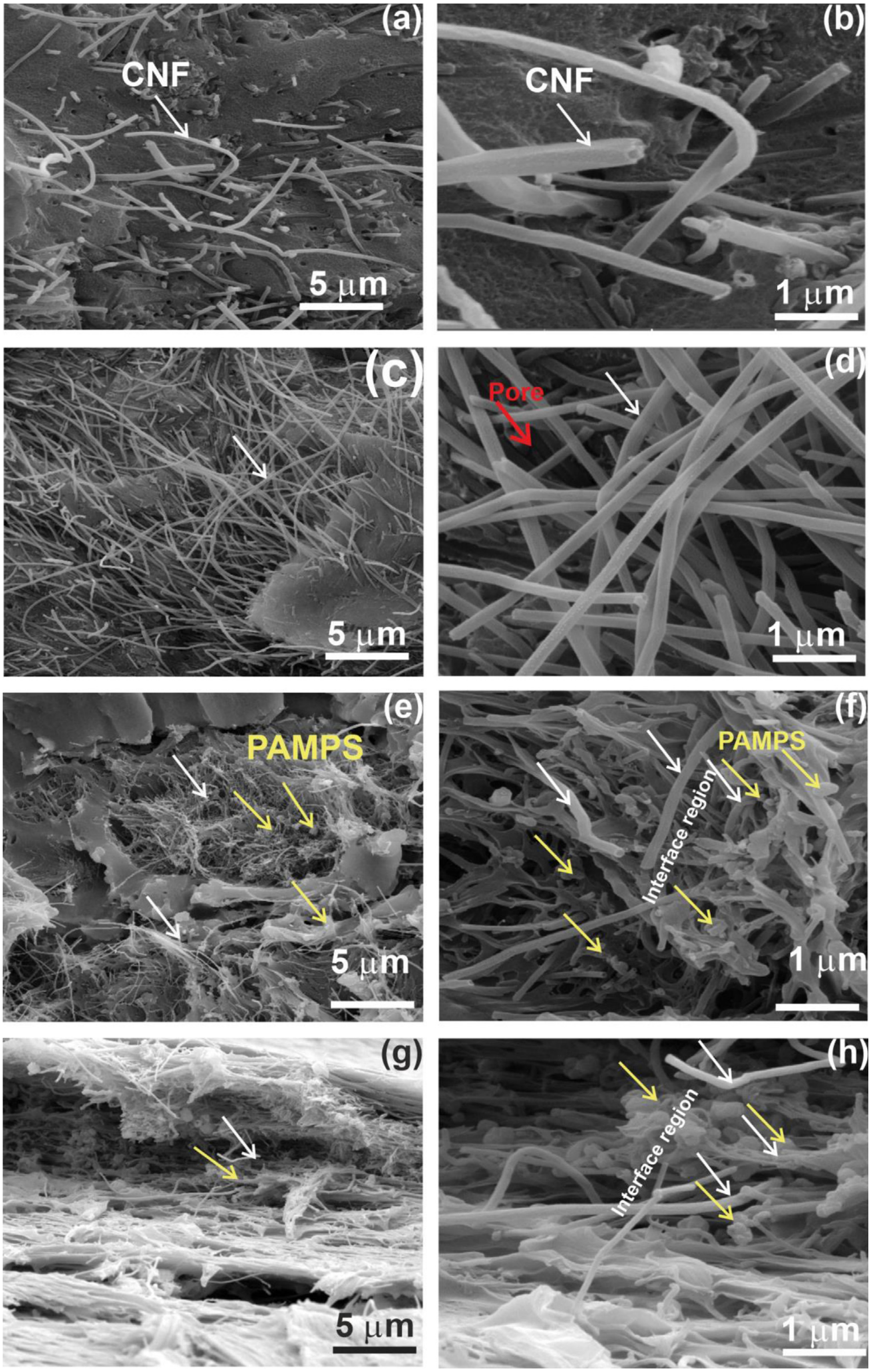

**Fig. 2 – Fractured SEM images of PHNC membrane of (a–b) 98/2/0, (c–d) 90/2/8, (e–f) 80/2/18, and (g–h) 70/2/28, in magnification of 5kX and 40kX, respectively.**

Figure 2(c)–2(d) show the cross-sectional SEM images of the PVDF/CNF/PAMPS (90/2/8) PHNC with a magnification of 5kX and 40kX, respectively, that exhibit a large porous structure between the CNF nanorods. The red arrow shows the pores on the sample surface. The PAMPS microbeads are not observed on the surface of 90/2/8 PHNC due to the low quantity of PAMPS. Figure 2(e)–2(f) show the cross-sectional SEM images of the 80/02/18 PHNC with a magnification of 5kX and

40kX, respectively. The yellow arrow shows the PAMPS microbeads in these images. From these figures, the interfacial interaction between CNF nanorods and PAMPS microbeads is observed in the backbone of PVDF. Figure 2(g)–2(h) show the cross-sectional SEM images of the 70/2/28 PHNC with a magnification of 5kX and 40kX, respectively. The SEM image of 70/2/28 PHNC also shows the interfacial interaction between CNF nanorods and PAMPS microbeads and is shown by the arrows. The interfacial interactions between the CNF nanorods and the PAMPS microbeads help the formation of continuous proton transfer paths, indicating that the sulfonic acid groups of PAMPS were evenly distributed on the surface of the PVDF/CNF/PAMPS PHNC for proton exchange. The pore development and uniform distribution of PAMPS beads in PVDF lead to strong intermolecular bonding between the polymer and the polyelectrolyte.

Furthermore, increasing PAMPS concentration in 80/02/18 and 70/2/28 PHNCs makes the pore density on the membrane's surface denser. This behavior is likely because CNF and PAMPS have relatively strong hydrogen bonding and interfacial interaction due to the electron donor properties of CNF and electron acceptor properties of PAMPS as observed by FTIR analysis. The interfacial interaction of CNF was observed with other polyelectrolytes [39,40,44]. With an increase in the concentration of PAMPS, numbers of sulphonic groups beads are attached to the carbon network, increasing the surface bonding and charge flow through the membrane. As a result, the existence of PAMPS and conductive filler CNF within the polymeric PVDF matrix has been seen in Fig. 2(e)–(h), which demonstrates strengthened allocation of PAMPS with CNF in PVDF film, which improves the electrical properties and β-phase content with greater flexibility and mechanical strength of PHNC membranes.

Fig. S3 shows the EDX SEM images and elemental mapping of 98/2/0, 90/2/8,80/2/18, and 70/2/28 PHNC that confirms the presence of C, O, F, and S elements. Figs. S3 (a)-i and ii show the SEM and EDX dot maps of the 98/2/0 based PHNC that display the 9%, 1%, 24%, and 1% of the C, O, F, and S dots, respectively. Figs. S3 (b)-i and ii show the SEM and EDX dot maps of the 90/2/8 based PHNC that display the 11%, 1%, 25%, and 1% of the C, O, F, and S dots, respectively. Figs. S3 (c)-i and ii show the SEM and EDX dot maps of the 80/2/18 based PHNC that display the 9%, 1%, 23%, and 1% of the C, O, F, and S dots, respectively. Fig. S3 (d)-i and ii show the SEM and EDX dot maps of the 70/2/28 based PHNC that display the 10%, 1%, 25%, and 1% of the C, O, F, and S dots, respectively.

The count of elements as a function of the X-ray energy is shown for 98/02/0, 90/02/08, 80/02/18, and 70/02/28 ratios PHNCs in the EDX spectrum Fig. S4 (a), (b), (c), and (d), respectively, and the elemental compositions were estimated as weight% and atomic% in Table S1, which indicates that the sample 90/2/0 shows the largest peak for F element. The sample 70/2/28 displays the high peaks for C, N, O, and S elements compared to the other blends.

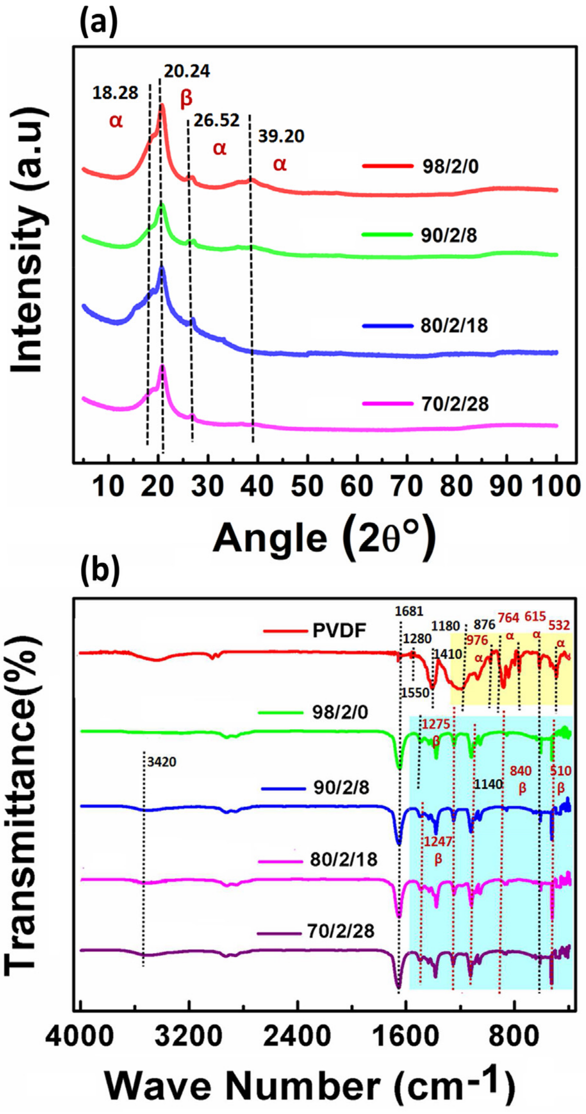

**Fig. 3 – (a) XRD and (b) FTIR spectra of PHNC.**

## 3.2. *XRD analysis of PHNCs*

X-Ray Diffraction (XRD) methods were employed to investigate the crystalline structure of the samples. Figure 3(a) shows a comparative analysis of XRD patterns of PHNC films produced using PVDF, CNF, and PAMPS. Past investigations of XRD of pure PVDF have shown that two intense diffraction peaks at 18.4 (020) and 20.0 (110), as well as a medium peak at 26.6 (021), reflects the monoclinic α-phase crystal, show that pure PVDF is mostly composed of the non-polar α-phase and indeed the pure PVDF functions as a dielectric material. The diffraction peaks of pure PVDF are wide enough, suggesting the semi-crystalline nature of the polymer [45,46]. In Fig. 3(a), when the CNF was combined with PVDF in sample 98/2/0 and to prepared the composite, a peak at $2\theta = 20.24^\circ$ and three weak peaks at $2\theta = 18.28$, 26.52, and 39.20 were observed. The peak at $2\theta = 20.24^\circ$ reflects the formation of polar β-phase on CNF insertion in PVDF, allowing easy charge transport in the whole membrane and is responsible for piezoelectricity and the three weak peaks at $2 = 18.28^\circ$, $26.5^\circ$, and $39.2^\circ$ show that there are few non-polar α-phase contents present. The stronger and narrower peak at $2\theta = 20.24^\circ$ represents the crystallinity of the polymer was enhanced by combining the graphitized CNF with PVDF.

Furthermore, the XRD spectra of PVDF/CNF/PAMPS membranes (sample 90/2/8, 80/2/18, 70/2/28) show a peak at $2\theta = 20.24^\circ$, indicating the presence of CNF. A weak peak at $2\theta = 26.52^\circ$, with the disappearance of the peak at $2\theta = 18.28^\circ$ and $39.20^\circ$ indicates the decreasing content of α-phase. Therefore, when PAMPS was inserted into PVDF, it only displayed peaks at $2\theta = 20.24^\circ$ in samples 90/2/8, 80/2/18, and 70/2/28, indicating that the concentration of piezoelectric β-phase of PVDF was improved due to the ions transmitted through PAMPS polyelectrolyte. It also demonstrates that PAMPS serves as an interface binder to alter the phase from α to β and that CNF contributes to increasing the electrical conductivity of the PVDF/PAMPS/CNF PHNC membranes. The degree of crystallinity of PHNC membranes of PVDF/CNF/PAMPS was 58.1%, which was 23.6% higher than pure PVDF membranes. Therefore, the inclusion of PAMPS leads to increase crystallinity in the PHNC membrane.

### 3.3. *FTIR analysis of PHNCs*

The corresponding FTIR spectrum (in Fig. 3(b)) agrees well with the XRD data, indicating a strong α-phase PVDF. There are two high-intensity peaks at 764 $cm^{-1}$ and 532 $cm^{-1}$ ascribed to non-polar α-phase and low-intensity peaks at 1275 $cm^{-1}$representing the polar β-phase of Crystal, representing piezoelectricity. In general, the FTIR transmittance peaks at 1275 $cm^{-1}$, 840 $cm^{-1}$, and 510 $cm^{-1}$ reflect the development of the piezoelectric β-phase, whereas the peaks at 532 $cm^{-1}$, 615 $cm^{-1}$, 764 $cm^{-1}$, and 976 $cm^{-1}$ in the FTIR spectrum are attributed to the non-polar α-phase in pristine PVDF [45–47].

FTIR Peaks observed at 1681 $cm^{-1}$, 1410 $cm^{-1}$, 1180 $cm^{-1}$, and 876 $cm^{-1}$ correspond to functional group C=O, C–F, C–C, and = C–H of pure PVDF, respectively. In contrast, a wide spectrum at 3450 $cm^{-1}$, 1140 $cm^{-1}$, 1550 $cm^{-1}$, and 1680 $cm^{-1}$ was detected in pure PAMPS, corresponding to –OH (-$SO_3H$), S–O, C–N, and C=O, which were missing in pure PVDF [42,48]. According to the FTIR figure, a similar peak was also observed at 3420 $cm^{-1}$ in PVDF/CNF/PAMPS-based PHNCs, i.e., this peak shifted from 3450 $cm^{-1}$ to 3420 $cm^{-1}$ for all PAMPS containing PHNCs, indicating that the vibration peak of the –OH band in PHNC expended more than pure PAMPS, confirming the creation of hydrogen bonding between CNF and PAMPS. Further, the band at 1280 $cm^{-1}$ in pure PVDF shifted to 1275 $cm^{-1}$ in the PVDF/CNF spectrum and shifted to 1247 $cm^{-1}$ in PVDF/CNF/PAMPSPHNCs, due to the vibration of the –$CH_2$ groups evidences a shift to 1247 $cm^{-1}$ in the spectrum of the 80/2/18 PHNC. This peak shift indicates a probable interfacial interaction between PAMPS, CNF, and the –$CF_2$ group of the PVDF matrix. As a result, the orientation of dipoles in the PVDF matrix contributes to the creation of the β-phase conformation. Figure 3(b) depicts a potential interaction mechanism of PAMPS trigger CNF and PVDF in the PHNCs.

The transmittance spectra of samples 98/2/0, 90/2/8, 80/2/18, and 70/2/28, as well as a spectrum of pure PVDF, are presented in Fig. 3(b). It was discovered that an identical peak (1140 $cm^{-1}$) was also detected in samples containing both CNF and PAMPS with PVDF, namely samples 98/2/0, 90/2/8, 80/2/18, and 70/2/28. With the addition of PAMPS to the PVDF/CNF compositions, the intensity of the peaks corresponding to α-phase progressively declines while the intensity of the peaks corresponding to β-phase (peaks at 510, 840, and 1247 $cm^{-1}$) gradually rises. In Table 1, the percentage fraction of β-phase F(β) in PHNC is enhanced. F(β) is 71.2 percent for PHNC with a 98/2/0 ratio. F(β) in PHNC, on the other hand, increases with the addition of PAMPS up to 18% and reaches a maximum value of 88.3 percent; after that, it decreases. As a result, gradually adding PAMPS to PVDF/CNF enhances the efficiency of the polar β-phase of PVDF, which is responsible for the piezoelectricity of PHNC membranes.

### 3.4. *DSC analysis (thermal analysis) of PHNCs*

Figure S5 depicts the DSC thermograph of PHNC samples. Pure PVDF has a melting temperature ($T_m$) of around 167 °C, ascribed to crystal-melt recrystallization [41]. The FTIR results indicate that 98/2/0, 90/2/8, 80/2/18, and 70/2/28 PHNC samples include β-crystals; also, the previous studies show the β-phase has a higher melting temperature value than that of the PVDF α-phases [49]. When CNF is added to PVDF, a new peak arises at a slightly higher temperature (167.75 °C), as seen in Fig S5, however when PAMPS is added to PHNC samples, a new peak occurs at a higher temperature, and as the concentration of PAMPS in PHNCs rises, the peak size grows. The melting peak at 170.49C for the 90/2/8 PHNC sample is due to the melting of the β-crystals in the PHNC. As a result, the higher value of melting peaks in the thermograms above can be referred to the β-phase PVDF. The melting temperatures of α-and β-phases of PHNC samples are also presented in Fig. S5, the first spike in $T_m$ with PAMPS content is owing to the excellent dispersion of CNF-PAMPS in PVDF matrix, which results in a dense and higher melting crystal. With increasing PAMPS, the melting temperature of the PHNC decreases (i.e the melting peak at 169.92 °C and 169.61 °C for 80/2/18, 70/2/28 PHNC sample respectively) which may be due to the particular interaction between CNF and PVDF matrix during the melt. As a result, PAMPS act as an excellent interfacial bonding material between CNF and the PVDF matrix, which is needed for

**Table 1 – %β-phase content, Crystallinity measurement of sample membranes from FTIR and DSC thermograph.**

| Sample Name | %β-phase FTIR | Onset melt Temp (C) | Melting Temp. (C) | $\Delta H_m$ (J/g) | Crystallinity ($X_c$) (%) |
|---|---|---|---|---|---|
| 98/2/0 | 71.2 | 148.60 | 167.75 | 59.87 | 57.30 |
| 90/2/8 | 84.6 | 151.51 | 170.49 | 60.12 | 57.53 |
| 80/2/18 | 88.3 | 152.80 | 169.92 | 60.69 | 57.99 |
| 70/2/28 | 86.2 | 148.70 | 169.61 | 60.36 | 57.76 |

homogeneous CNF dispersion in the PVDF matrix. All PHNC samples had a crystallinity of ~58%, indicating that the crystallinity had been maintained, which is approximately equal (~58.1%) to the crystallinity measured by XRD patterns. The crystallinity of the 98/2/0, 90/2/8, 80/2/18, and 90/2/28 ratios PHNC samples are 57.30%, 57.53%, 57.99% and 57.76% respectively. It can be considered β phase is more crystalline as compared to α phase of PVDF. Hence, PAMPS grafted CNF has more ability to strengthen the β phase in the PVDF matrix because of high crystallinity. As a result of the interactions of PAMPS and CNF in the polymer, the interfacial bonding is stronger in the crystalline phase, the polymer's crystallinity increases, and the mechanical properties of the samples membrane improve. Table 1 summarizes the melting enthalpie ($H_m$), melting temperature ($T_m$) and crystallinity ($X_c$) determined from the DSC spectrum.

### 3.5. *Mechanical analysis of PHNCs*

The mechanical properties of the PHNC sample, such as tensile strength, Young's modulus, bending stiffness, and flexibility, have been investigated by the stress–strain curve shown in Fig. 4. The highest point of the stress–strain curve represents a tensile strength of the material; hence, sample 98/2/0 demonstrated the maximum tensile strength of 52.2 MPa in comparison to others shown in Fig. 4(b). The elongation on the stress–strain curve represents a fracture or brittle point of materials, so the higher elongation of the stress–strain curve shows more ductile or flexible material, from Fig. 4(a). In comparison to the others, sample 80/2/18 is the most ductile, while sample 98/2/0 is brittle because sample 80/2/18 has the most elongation, while 98/2/0 has the least. The lack of PAMPS in sample 98/2/0 is noteworthy because the elongation of samples improved with increasing PAMPS concentration. It should be noted that the excessive PAMPS doping (>18 wt%) limited the elongation of the composite film; therefore, elongation of 70/2/28 is declining as it sustains less elongation just before failure shown in Fig. 4(c).

The bending stiffness of the sensing membrane is measured using Young's modulus, which is described as the ratio of stress along an axis to strain. The bending stiffness ($B$) for a PHNC membrane; $B = EI/b$, where $E$ indicates Young's modulus, and $I$ represent the moment of inertia of flexible membrane [12]. A high flexible material has a low Young's modulus. Young's modulus results for PVDF/CNF/PAMPS PHNC membrane with PAMPS content of 0 wt%, 8 wt%, 18 wt %, and 28wt% were 1962.40 MPa, 1179.01 MPa, 803.36 MPa, and 558.944 MPa, respectively, as shown in Fig. 4(d). With a PAMPS

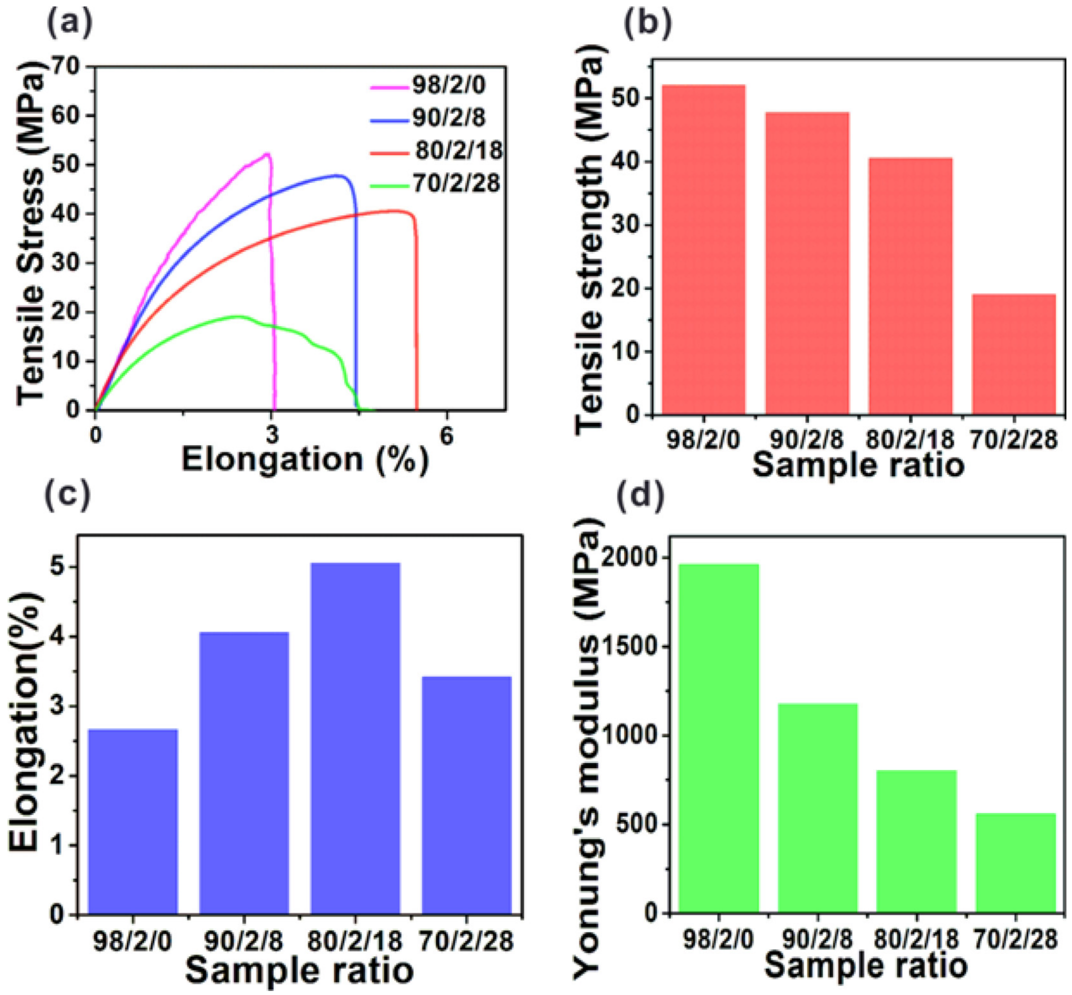

**Fig. 4 – (a) Stress–Strain Curve, (b) Tensile strength, (c) Elongation, and (d) Young modulus of PHNC membranes.**

concentration of 28 wt% in sample 70/2/28, the bending stiffness of PVDF/CNF/PAMPS membrane is predicted to be higher, and Young's modulus will be lower, making 70/2/28 more flexible.

### 3.6. *Electrical parameters analysis of PHNCs*

The graph of dielectric constant ($\varepsilon$) and dielectric loss (*tan* $\delta$) of all nanocomposite piezoelectric membranes with frequency comprising 98/2/0, 90/2/8, 80/2/18, and 70/2/28 are shown in Fig. 5(a) and dielectric loss (*tan* $\delta$) of all PHNC membranes shown in Fig. S6(a). Due to the material's polarization effect, all samples showed a reduction in the attributes of dielectric constant ($\varepsilon$) and dielectric loss (*tan* $\delta$) as the frequency increased. The polarization of atoms tends to follow the frequencies at lower frequencies but not at higher frequencies, which decreases the attributes of dielectric constant ($\varepsilon$) and dielectric loss (*tan* $\delta$). Sample 80/2/18 had the greatest attributes of dielectric constant ($\varepsilon$) and dielectric loss (*tan* $\delta$) because of the uniform dispensation of the filler CNF and polyelectrolyte PAMPS with PVDF (in Fig. 2(e-f)), which increased the dipole-moment in the sample 80/2/18.

The concentration of PAMPS in sample 70/2/28 was high, which resulted in agglomeration (see Fig. 2(g-h)), which terminated the polarization of charge carriers and dropped the $\varepsilon$ and *tan* $\delta$. Since ac conductivity ($\sigma_{ac}$) is proportional to dielectric constant ($\varepsilon$) and dielectric loss (tan $\delta$), ac conductivity ($\sigma_{ac}$) of all PHNC samples showed identical behavior with frequency as dielectric constant ($\varepsilon$) and dielectric loss (tan $\delta$) shown in Fig. 5(b) and Fig. S6(a). For sample 80/2/18, the maximum value of $\sigma_{ac}$ was attained with frequency. The change in capacitance of the samples caused by changing the concentration of PAMPS in the presence of CNF is ascribed to the properties displayed by the dielectric constant ($\varepsilon$) and dielectric loss (tan $\delta$), confirming PAMPS as a suitable ionic binder.

To calculate the dc conductivity of PVDF/CNF/PAMPS PHNC membrane, imaginary impedance ($Z''$) versus real impedance ($Z'$) plot for ratio 98/2/0, 90/2/8, 80/2/18, and 70/2/28 is shown in Fig. 5(c) and (d); and broad-frequency range for 80/2/18, and 70/2/28 is shown in Fig.S6(b). The dc resistance of various PHNC membranes is examined in the high-frequency range to calculate the dc conductivity. Due to the maximum dc conductivity of this composition, the 80/2/18 PHNC membrane has the lowest resistance ($R = 73\ \Omega$) of the other compositions. This implies the highest conductivity of the 80/2/18 blend than that of the other blends (shown in Table 2).

### 3.7. *Electrochemical analysis (water uptake) of PHNCs*

The water uptake (WUP) and contact angle were used to investigate the hydrophilic nature of the various PHNC

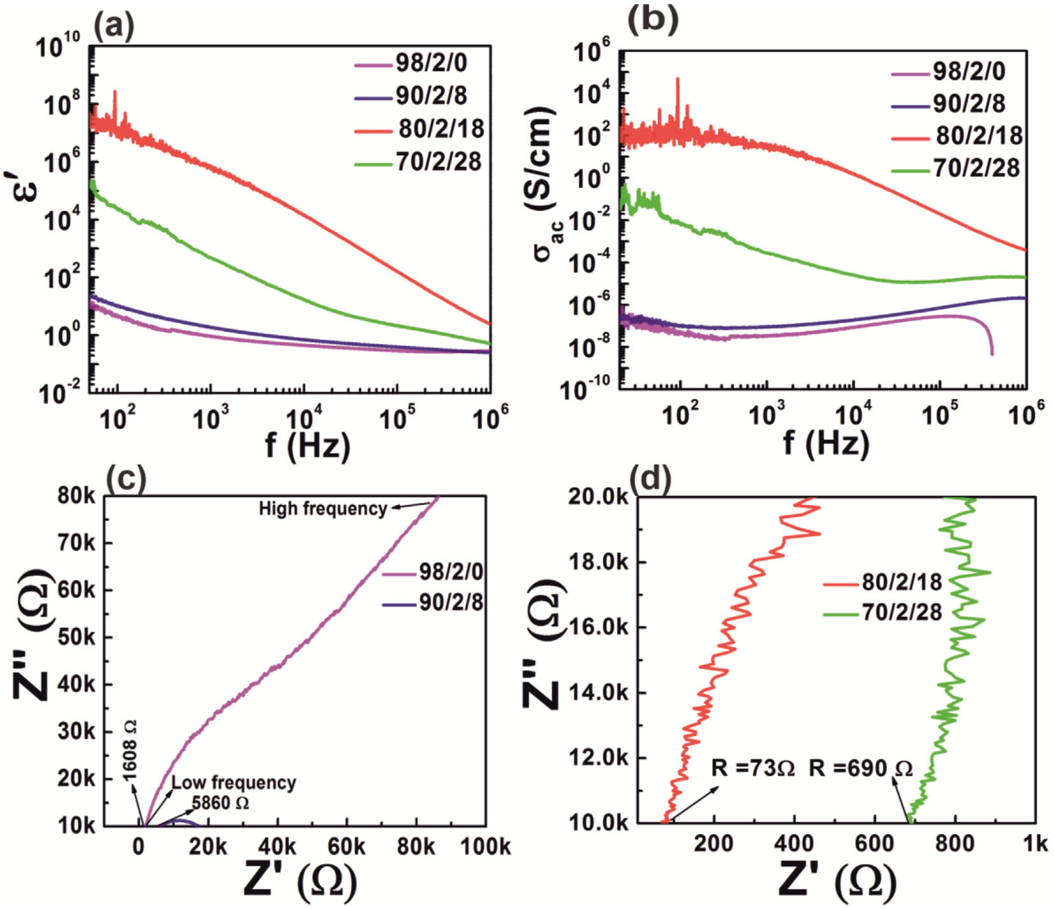

**Fig. 5 – (a) Dielectric constant ($\varepsilon$) of PHNC, (b) AC conductivity ($\sigma_{ac}$) of PHNC membranes, (c) Nyquist plot of PHNC of ratio 98/2/0 and 90/2/8, and (d) Nyquist plot of PHNC of ratio 80/2/18 and 70/2/28.**

**Table 2 – Electrochemical and electrical properties of PHNC membranes.**

| Sensing Membrane Ratio | WUP | Contact Angle | dc conductivity (S/cm) | Capacitance (mF) |
|---|---|---|---|---|
| 98/2/0 | 0.102 | 70.2° | 0.019805 | 0.124 |
| 90/2/8 | 0.121 | 62.4° | 0.005434 | 0.181 |
| 80/2/18 | 0.228 | 55.8° | 0.436262 | 0.183 |
| 70/2/28 | 0.203 | 47.8° | 0.046155 | 0.180 |

membranes. The Contact angle of the PHNC membrane surface is measured by dropping a deionized water droplet over the membrane surface and measured using a goniometer. Figure 6(a), (b), (c), and (d) illustrates the contact angle for 98/2/0, 90/2/8, 80/2/28, and 70/2/18 PHNC blends, which are 70.2°, 62.4°, 55.8°, and 47.8°, respectively. A lower contact angle from the surface of the PHNC blend implies hydrophilic nature. The 70/2/28 based PHNC membrane shows the lowest contact angle of 47.8° implying the highest WUP (0.228) compared to the other blends of 98/2/0, 90/2/8, and 80/2/18, owing to the highest water absorber and PAMPS content. The 98/02/0 based PHNC membrane exhibits the highest contact angle (70.2°) and a lowest WUP value (0.102) than that of 90/2/8, 80/2/18, and 70/2/28 blends. The value below 90° of the contact angle confirms the hydrophilic behavior of the PHNC membrane. The hydrophilic nature of PHNCs signifies that the dispersion of CNF in the PVDF matrix has been improved due to the presence of PAMPS [50]. Also, the contact angles have been reduced from 70.2° to 47.8°, which implies that the porosity of the PHNC membrane is enhanced, as shown in Fig. 2, which improves the electrical and sensing performance (shown in Table S2).

## 3.8. *Piezoelectric performance of PHNCs*

By bending the PHNC sample on the bending machine for several bending cycles, the piezoelectric sensing capability of PHNC membranes was investigated. The PHNC membranes were bent and released repeatedly under a compressive force of 9 N, which corresponded to mechanical stress of 0.09 MPa. As a result, the output voltage is generated. To study the piezoelectric capability of PHNCs, a series of PHNCs with different PAMPS weight ratios, namely 0, 8, 18, and 28 wt%, were developed and the output voltage was recorded using the same technique under the repeated bending-releasing procedure. The maximum peak output voltages of 98/2/0, 90/2/8, 80/2/18, and 70/2/28 PHNCs were 0.62 V, 1.20 V, 3.65 V, and 2.34 V, respectively, as shown in Fig. 7(a), which exhibits the outstanding repeatability of the PHNCs for sensing applications. Fig. S7 shows digital images of PHNC membrane sensing performance with 0.009 bending strain. Table S2 shows the maximum peak piezoelectric voltage of all PHNCs after WUP.

Figure 7(b) shows that the piezoelectric maximum peak output voltage in PHNCs increases in direct proportion to the concentration of PAMPS, which can be ascribed to increased

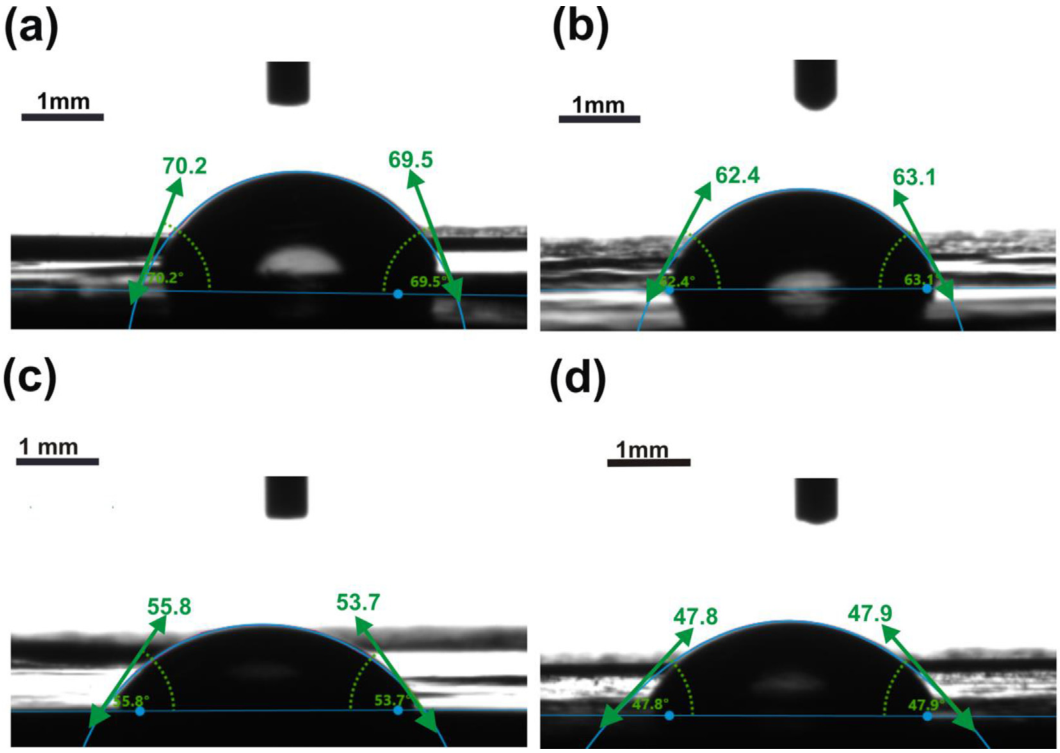

**Fig. 6 – Contact angles of PHNC membranes with different sample ratio: (a) 98/2/0, (b) 90/2/9, (c) 80/2/18, and (d) 70/2/28.**

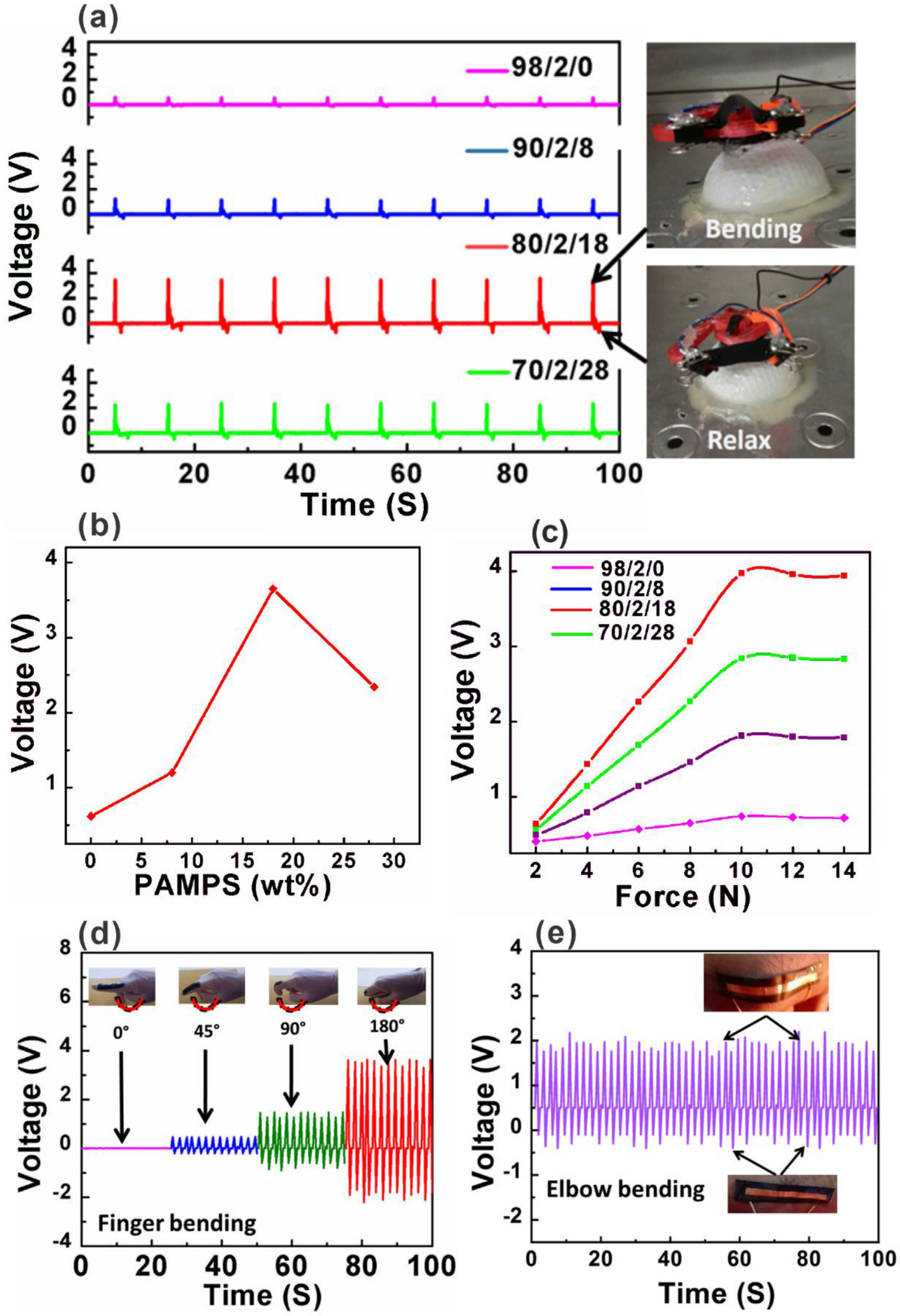

**Fig. 7 – (a) Output sensing voltages of PHNCs on bending machine with different sample ratio, (b) output voltage vs % wt of PAMPS, (c) output voltage vs applied force, (d) human motion sensor for a finger at various angles using PHNC with 80/2/18 sample ratio, and (e) human motion sensor for an elbow movement.**

piezoelectricity. The concentration of PAMPS in sample 70/2/28 was high as 28 wt%, which resulted in agglomeration (see Fig. 2(e-f)) and comparatively low elongation than sample 80/2/18 (see Fig. 4(c)), which reduced the polarization of charge particles and dropped the dielectric constant and conductivity of PHNC membrane. Hence, the desirable piezoelectric β-phase of PVDF decreases, and output voltage becomes low (highest recorded peak values reaching 2.34 V) than that of 80/

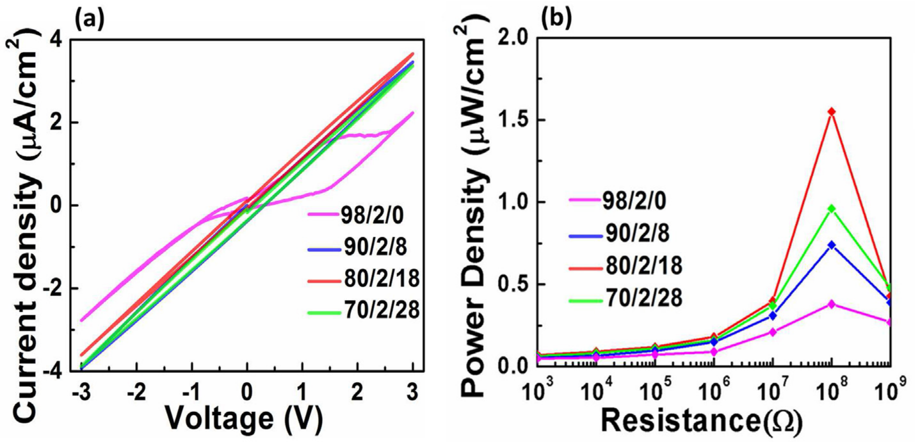

**Fig. 8 – (a) Cyclic current–voltage analysis, (b) Power density of PHNC with different sample ratio.**

2/18. As a result, a simple, efficient, and cost-effective technique may be used to produce high-performance PVDF/CNF/PAMPS with 18 wt% PAMPS nanocomposite piezoelectric membranes using our approach. The piezoelectric nature of PHNCs with converse connections is shown in Fig. S8.

The sensitivity test of all PHNC is shown in Fig. 7(c), with applied force ranging from 2 to 14 N. The maximum peak voltage output from PHNCs with ratios of 98/2/0, 90/2/8, 80/2/18, and 70/2/28 was 0.74 V, 1.81 V, 3.87 V, and 2.84 V, respectively. Compared to the other three PHNCs, the 80/2/18 PHNC produces the highest peak voltage output under identical operating circumstances. With increasing applied force, the piezoelectric output voltage generated by all PHNCs grows linearly. This causes stronger compressive forces on piezoelectric materials, resulting in higher charge deformations, as shown in Fig. 7(c). As a result, the 80/2/18 PHNC achieved the greatest sensitivity of 0.38 V/N, demonstrating superiority over different PVDF-based piezoelectric sensors, which is excellent among the reported PVDF-based sensors [51]. The linearity and sensitivity of the PHNC decline beyond 10 N, hence the sensing range of this PHNC is up to 10 N.

The piezoelectric performance of PVDF/CNF/PAMPS PHNC was also evaluated using a human motion test. Figure 7(d) shows the generated voltage from 80/2/18 based PHNC placed on the index finger at different angles. The output piezoelectric voltage response was induced when the index finger was periodically bent and straightened. With the degree of bending of the index finger, the generated piezoelectric output voltage increased, and the voltage reached a maximum of approximately 0.45 V, 1.62 V, and 3.58 V at 45°, 90°, and 180°, respectively. Furthermore, following elbow bending Fig. 7(e), this 80/2/18 based PHNC generates around 2 V repeatedly, demonstrating the outstanding repeatability of this PHNC; as a result, this PHNC is suited for harvesting energy from small human movements, as well as promising for a variety of sensing applications with high sensitivity.

The reproducibility test of the PHNC was carried out over two weeks using the bending and releasing procedure under the force of 9 N using a bending machine. Figure S9 (a) shows the maximum peak output voltage of 3.6 V for 80/2/18 based PHNC. There are no noticeable variations after 3600 cycles in 1 h, showing that the PHNC is capable of long-term operation. In addition, in the second week, the reproducibility of the 80/2/18 based PHNC was tested for additional 3600 cycles under identical circumstances (see in Fig. S9(b)). Compared to the first week's measurement, the results demonstrate constant output voltage with no obvious deterioration. That confirms the exceptional reproductively in PHNC.

Furthermore, using the PHNC, we can efficiently check the abnormal motion of human joints caused by injuries. PHNCs can also monitor the situations of patients with Parkinson's disease and quantify the recovery of those with a joint injury, implying a huge potential for healthcare applications. The PHNC's response time was less than 100 ms. Rapid response ensured that the PHNC could catch the signals quickly, even under the external mechanical stimulus. Moreover, the 80/2/18 ratio PHNC membrane was repeatedly bent and released in over a wide temperature range from 20 °C to 100 °C; resulting in the generation of approximate constant maximum peak output piezoelectric voltage 3.65 V till 100 °C; that confirms excellent thermal stability of PHNC, shown in Fig. S10 of supplementary file. These findings indicated that the PHNC has benefits such as high sensitivity to external stimuli, superior flexibility, and a rapid reaction time, indicating the PHNC's tremendous potential in wearable health monitoring.

### 3.9. *Cyclic current -voltage (CV) analysis of PHNCs*

Using cyclic voltammetry, the electrical current density of a LiCl-dipped PVDF/CNF/PAMPS PHNC membrane was investigated shown in Fig. 8(a), which is essential for sensing applications. The dissipated electric current density of the 98/2/0, 90/2/8, 80/2/18, and 70/2/28 are found to be 2.22 μA/ cm$^2$, 3.42 μA/ cm$^2$, 3.64 μA/ cm$^2$ and 3.34 μA/ cm$^2$, respectively. The cyclic current density–voltage graph was also used to determine the capacitance of the PHNC membrane. The 98/2/0, 90/2/8, 80/2/18, and 70/2/28 PHNC membranes have capacitances of 0.124 mF, 0.183 mF, 0.181 mF, and 0.180 mF, respectively. As can be observed, the PVDF/CNF/PAMPS PHNC membrane exhibited high electrical current and capacitance values compared to the PVDF/CNF based PHNC membrane. This is due to the strong anionic polyelectrolyte property of PAMPS;

**Table 3 – Comparison of the sensing parameters of various piezoelectric sensors.**

| PHNC Membranes | Maximum Peak Voltage (V) | Electric Current density ($\mu$A/ cm$^2$) | Power density ($\mu$W/ cm$^2$) | Reference |
|---|---|---|---|---|
| PVDF/CNF/PAMPS: 98/2/0 | 0.62 | 2.22 | 0.38 | This work |
| PVDF/CNF/PAMPS: 90/2/8 | 1.20 | 3.42 | 0.74 | This work |
| PVDF/CNF/PAMPS: 80/2/18 | 3.65 | 3.64 | 1.55 | This work |
| PVDF/CNF/PAMPS: 70/2/28 | 2.34 | 3.34 | 0.96 | This work |
| PVDF/GO | 0.9 | 0.969 | NA | [37] |
| PVDF/rGO | 1.3 | 1.364 | NA | [37] |
| Diphenylalanine peptides | 1.4 | NA | NA | [52] |
| Diphenylalanine peptides | 2.2 | NA | NA | [25] |
| Diphenylalanine peptides/CNT | 2.8 | NA | NA | [53] |

when PAMPS is added to the membrane, the interfacial contact between CNF conductive fillers and PVDF molecular chains increases. It enables convenient ion transport across the CNF conductive nanorods in the whole membrane. As a result, polarization increases in the membrane; the piezoelectric β-phase of PVDF was improved. The comparison of different sensing parameters of PVDF/CNF/PAMPS PHNC with previously reported flexible piezoelectric sensors is shown in Table 3. It was found that the PVDF/CNF/PAMPS PHNC showed higher sensing voltage than previous existing flexible piezoelectric nanocomposite film sensors. The sensing properties of all PHNCs after the WUP are mentioned in Table S2. The power density of PHNCs is computed using formula $P = V^2/(R_L \times A)$, where P is the power density, V is the maximum output voltage, $R_L$ is the load resistance, and A is the PHNCs area. The power density of the PHNCs increases with an increase in the concentration of PAMPS (after 18% wt% of PAMPS power reduces) as shown in Fig. 8(b), and maximum power density is exhibited by 80/2/18 ratio PHNC of 1.55 $\mu$W/cm$^2$ with a maximum peak voltage of 3.65 V.

## 4. Conclusion

In conclusion, we proposed a new method for fabricating high-performance flexible piezoelectric nanocomposite (PHNC) membrane using PVDF/CNF/PAMPS for large-scale manufacturing and low-cost wearable devices. The polar β-phase of PVDF/CNF/PAMPS PHNC nanocomposite was produced due to the intermolecular bonding of PAMPS ions with CNF and PVDF using a solvent casting process that helps to generate piezoelectric nanocomposite. The PVDF/CNF/PAMPS nanocomposite with a ratio of 80/2/18 shows its energy harvesting ability by bending the PHNC sample on the bending machine for several bending cycles. The PHNC generates the maximum peak output voltage up to 3.65 V under the repeated bending-releasing procedure. Furthermore, wearable sensor application is demonstrated by exposing it to different human body movements such as finger and elbow movements. It generated maximum peak output voltage up to 3.58 V and 2.2 V at a bending angle of 180° for finger and elbow movements, respectively. The PHNC exhibits outstanding reproducibility and reliability for sensing applications. Due to the high voltage and flexible nature of the PVDF/CNF/PAMPS PHNCs, they could be used as health monitoring devices and nanogenerators for wearable electronic devices.

## Declaration of Competing Interest

The authors declare that they have no known competing financial interests or personal relationships that could have appeared to influence the work reported in this paper.

## Acknowledgments

The present research was financially supported by the Science and Engineering Research Board (SERB) [ECR/2016/001113] Government of India. Gopinathan Anoop wishes to thank the support of the Basic Science Research Program through the National Research Foundation (NRF) funded by the Ministry of Education (NRF-2020R1I1A1A01054253), Republic of Korea. Sukho Park wishes to thank the support of the National Research Foundation (NRF) funded by the Ministry of Science and ICT (NRF-2021R1A2C3007817), Republic of Korea.

## Appendix A. Supplementary data

Supplementary data to this article can be found online at https://doi.org/10.1016/j.jmrt.2022.02.075.

## REFERENCES

[1] Amjadi M, Kyung KU, Park I, Sitti M. Stretchable, skin-mountable, and wearable strain sensors and their potential applications: a review. Adv Funct Mater 2016;26:1678–98. https://doi.org/10.1002/adfm.201504755.

[2] Huang Y, Fan X, Chen SC, Zhao N. Emerging Technologies of flexible pressure sensors: materials, modeling, devices, and manufacturing. Adv Funct Mater 2019;29. https://doi.org/10.1002/adfm.201808509.

[3] Chang Y, Zuo J, Zhang H, Duan X. State-of-the-art and recent developments in micro/nanoscale pressure sensors for smart wearable devices and health monitoring systems. Nami Jishu Yu Jingmi Gongcheng/Nanotechnology Precis Eng 2020;3:43–52. https://doi.org/10.1016/j.npe.2019.12.006.

[4] Gao W, Ota H, Kiriya D, Takei K, Javey A. Flexible electronics toward wearable sensing. Acc Chem Res 2019;52:523–33. https://doi.org/10.1021/acs.accounts.8b00500.

[5] Wang Y, Wang L, Yang T, Li X, Zang X, Zhu M, et al. Wearable and highly sensitive graphene strain sensors for human

motion monitoring. Adv Funct Mater 2014;24:4666–70. https://doi.org/10.1002/adfm.201400379.

[6] Liao X, Liao Q, Yan X, Liang Q, Si H, Li M, et al. Flexible and highly sensitive strain sensors fabricated by pencil drawn for wearable monitor. Adv Funct Mater 2015;25:2395–401. https://doi.org/10.1002/adfm.201500094.

[7] Yan Z, Wang L, Xia Y, Qiu R, Liu W, Wu M, et al. Flexible high-resolution triboelectric sensor array based on patterned laser-induced graphene for self-powered real-time tactile sensing. Adv Funct Mater 2021;31:1–9. https://doi.org/10.1002/adfm.202100709.

[8] Duan Z, Jiang Y, Huang Q, Wang S, Wang Y, Pan H, et al. Paper and carbon ink enabled low-cost, eco-friendly, flexible, multifunctional pressure and humidity sensors. Smart Mater Struct 2021;30:055012. https://doi.org/10.1088/1361-665X/abe87d.

[9] Duan Z, Jiang Y, Huang Q, Yuan Z, Zhao Q, Wang S, et al. A do-it-yourself approach to achieving a flexible pressure sensor using daily use materials. J Mater Chem C 2021;9:13659–67. https://doi.org/10.1039/d1tc03102c.

[10] Tai H, Duan Z, Wang Y, Wang S, Jiang Y. Paper-based sensors for gas, humidity, and strain detections: a review. ACS Appl Mater Interfaces 2020;12:31037–53. https://doi.org/10.1021/acsami.0c06435.

[11] Duan Z, Jiang Y, Huang Q, Wang S, Zhao Q, Zhang Y, et al. Facilely constructed two-sided microstructure interfaces between electrodes and cellulose paper active layer: eco-friendly, low-cost and high-performance piezoresistive sensor. Cellulose 2021;28:6389–402. https://doi.org/10.1007/s10570-021-03913-8.

[12] Huang Q, Jiang Y, Duan Z, Yuan Z, Liu B, Zhang Y, et al. Protrusion microstructure-induced sensitivity enhancement for zinc oxide–carbon nanotube flexible pressure sensors. ACS Appl Electron Mater 2021;3:5506–13. https://doi.org/10.1021/acsaelm.1c00930.

[13] Xu F, Li X, Shi Y, Li L, Wang W, He L, et al. Recent developments for flexible pressure sensors: a review. Micromachines 2018;9. https://doi.org/10.3390/mi9110580.

[14] Zang Y, Zhang F, Di CA, Zhu D. Advances of flexible pressure sensors toward artificial intelligence and health care applications. Mater Horizons 2015;2:140–56. https://doi.org/10.1039/c4mh00147h.

[15] Senthil Kumar K, Xu Z, Sivaperuman Kalairaj M, Ponraj G, Huang H, Ng CF, et al. Stretchable capacitive pressure sensing sleeve deployable onto catheter balloons towards continuous intra-abdominal pressure monitoring. Biosensors 2021;11. https://doi.org/10.3390/bios11050156.

[16] Panwar LS, Panwar V, Panwar SS. Performance enhancement of pzt wearable blood pressure sensor using cantilever structure. Proc - 2020 Int Conf Adv Comput Commun Mater ICACCM 2020;2020:148. https://doi.org/10.1109/ICACCM50413.2020.9212895. 53.

[17] Wixom AS, Anderson MJ, Bahr DF, Morris DJ. A new acoustic transducer with a pressure-deformed piezoelectric diaphragm. Sensors Actuators, A Phys 2012;179:204–10. https://doi.org/10.1016/j.sna.2012.03.001.

[18] Fu J, Hou Y, Zheng M, Zhu M. Flexible piezoelectric energy harvester with extremely high power generation capability by sandwich structure design strategy. ACS Appl Mater Interfac 2020;12:9766–74. https://doi.org/10.1021/acsami.9b21201.

[19] Li Y, Xu M, Xia Y, Wu J, Sun X, Wang S, et al. Multilayer assembly of electrospun/electrosprayed PVDF-based nanofibers and beads with enhanced piezoelectricity and high sensitivity. Chem Eng J 2020;388. https://doi.org/10.1016/j.cej.2020.124205.

[20] Panwar LS, Kala S, Panwar V, Panwar SS, Sharma S. Design of MEMS piezoelectric blood pressure sensor. 3rd Int Conf Adv Comput Commun Autom 2017:1–7. https://doi.org/10.1109/ICACCAF.2017.8344698.

[21] Wan C, Bowen CR. Multiscale-structuring of polyvinylidene fluoride for energy harvesting: the impact of molecular-, micro- and macro-structure. J Mater Chem 2017;5:3091–128. https://doi.org/10.1039/c6ta09590a.

[22] Ruan L, Yao X, Chang Y, Zhou L, Qin G, Zhang X. Properties and applications of the β phase poly(vinylidene fluoride). Polymers 2018;10. https://doi.org/10.3390/polym10030228.

[23] Li Q, Zhao J, He B, Hu Z. Solution processable poly(vinylidene fluoride)-based ferroelectric polymers for flexible electronics. Apl Mater 2021;9. https://doi.org/10.1063/5.0035539.

[24] Low YKA, Meenubharathi N, Niphadkar ND, Boey FYC, Ng KW. In: Journal of biomaterials science , α - and β -poly (vinylidene fluoride) evoke different cellular behaviours; 2012. p. 1651–67.

[25] Nguyen V, Kelly S, Yang R. Piezoelectric peptide-based nanogenerator enhanced by single-electrode triboelectric nanogenerator. Apl Mater 2017;5. https://doi.org/10.1063/1.4983701.

[26] Hu X, Yan X, Gong L, Wang F, Xu Y, Feng L, et al. Improved piezoelectric sensing performance of P(VDF-TrFE) nanofibers by utilizing BTO nanoparticles and penetrated electrodes. ACS Appl Mater Interfac 2019;11:7379–86. https://doi.org/10.1021/acsami.8b19824.

[27] Sahu M, Hajra S, Lee K, Deepti P, Mistewicz K, Kim HJ. Piezoelectric nanogenerator based on lead-free flexible pvdf-barium titanate composite films for driving low power electronics. Crystals 2021;11:1–10. https://doi.org/10.3390/cryst11020085.

[28] Wang Y, Yao M, Ma R, Yuan Q, Yang D, Cui B, et al. Design strategy of barium titanate/polyvinylidene fluoride-based nanocomposite films for high energy storage. J Mater Chem 2020;8:884–917. https://doi.org/10.1039/c9ta11527g.

[29] Chandran AM, Varun S, Mural PKS. Flexible electroactive PVDF/ZnO nanocomposite with high output power and current density. Polym Eng Sci 2021;61:1829–41. https://doi.org/10.1002/pen.25704.

[30] Dossin Zanrosso C, Piazza D, Lansarin MA. PVDF/ZnO composite films for photocatalysis: a comparative study of solution mixing and melt blending methods. Polym Eng Sci 2020;60:1146–57. https://doi.org/10.1002/pen.25368.

[31] Surmenev RA, Chernozem RV, Pariy IO, Surmeneva MA. A review on piezo- and pyroelectric responses of flexible nano- and micropatterned polymer surfaces for biomedical sensing and energy harvesting applications. Nano Energy 2021;79:105442. https://doi.org/10.1016/J.NANOEN.2020.105442.

[32] Li B, Xu C, Zheng J, Xu C. Sensitivity of pressure sensors enhanced by doping silver nanowires. Sensors 2014;14:9889–99. https://doi.org/10.3390/s140609889.

[33] Cheon S, Kang H, Kim H, Son Y, Lee JY, Shin HJ, et al. High-performance triboelectric nanogenerators based on electrospun polyvinylidene fluoride–silver nanowire composite nanofibers. Adv Funct Mater 2018;28:1–7. https://doi.org/10.1002/adfm.201703778.

[34] Zhang H, Zhu Y, Li L. Fabrication of PVDF/graphene composites with enhanced β phase: via conventional melt processing assisted by solid state shear milling technology. RSC Adv 2020;10:3391–401. https://doi.org/10.1039/c9ra09459h.

[35] Liu X, Ma J, Wu X, Lin L, Wang X. Polymeric nanofibers with ultrahigh piezoelectricity via self-orientation of nanocrystals. ACS Nano 2017;11:1901–10. https://doi.org/10.1021/acsnano.6b07961.

[36] Roy K, Ghosh SK, Sultana A, Garain S, Xie M, Bowen CR, et al. A self-powered wearable pressure sensor and pyroelectric breathing sensor based on GO interfaced PVDF nanofibers.

ACS Appl Nano Mater 2019;2:2013. https://doi.org/10.1021/acsanm.9b00033. 25.

[37] Ataur Rahman M, Lee BC, Phan DT, Chung GS. Fabrication and characterization of highly efficient flexible energy harvesters using PVDF-graphene nanocomposites. Smart Mater Struct 2013;22. https://doi.org/10.1088/0964-1726/22/8/085017.

[38] Yu S, Zheng W, Yu W, Zhang Y, Jiang Q, Zhao Z. Formation mechanism of β-phase in PVDF/CNT composite prepared by the sonication method. Macromolecules 2009;42:8870–4. https://doi.org/10.1021/ma901765j.

[39] Prasad B, Gill FS, Panwar V, Anoop G. Development of strain sensor using conductive poly(vinylidene fluoride) (PVDF) nanocomposite membrane reinforced with ionic liquid (IL) & carbon nanofiber (CNF). Compos B Eng 2019;173. https://doi.org/10.1016/j.compositesb.2019.106990.

[40] Kaur Prabhsharan, Shin Mun-Sik, Park Jin-Soo, Gaurav Verma SSS. Supramolecular modification of Carbon Nanofibers with Poly(diallyl dimethylammonium) chloride and Triton X-100 for electrochemical application. Int J Hydrogen Energy 2018;43:6575–85. https://doi.org/10.1016/j.ijhydene.2018.02.075.

[41] Mandal A, Nandi AK. Ionic liquid integrated multiwalled carbon nanotube in a poly(vinylidene fluoride) matrix: formation of a piezoelectric β-polymorph with significant reinforcement and conductivity improvement. ACS Appl Mater Interfaces 2013;5:747–60. https://doi.org/10.1021/am302275b.

[42] Son YJ, Kim SJ, Kim YJ, Jung KH. Selective vapor permeation behavior of crosslinked PAMPS membranes. Polymers 2020;12. https://doi.org/10.3390/POLYM12040987.

[43] Sencadas V, Martins P, Pitães A, Benelmekki M, Gómez Ribelles JL, Lanceros-Mendez S. Influence of ferrite nanoparticle type and content on the crystallization kinetics and electroactive phase nucleation of poly(vinylidene fluoride). Langmuir 2011;27:7241–9. https://doi.org/10.1021/la2008864.

[44] Chaturvedi M, Panwar V, Prasad B. Piezoresistive sensitivity tuning using polyelectrolyte as interface linker in carbon based polymer composites. Sensors Actuators, A Phys 2020;312:112151. https://doi.org/10.1016/j.sna.2020.112151.

[45] Cai X, Lei T, Sun D, Lin L. A critical analysis of the α, β and γ phases in poly(vinylidene fluoride) using FTIR. RSC Adv 2017;7:15382–9. https://doi.org/10.1039/c7ra01267e.

[46] Nishiyama T, Sumihara T, Sasaki Y, Sato E, Yamato M, Horibe H. Crystalline structure control of poly(vinylidene fluoride) films with the antisolvent addition method. Polym J 2016;48:1035–8. https://doi.org/10.1038/pj.2016.62.

[47] Bai H, Wang X, Zhou Y, Zhang L. Preparation and characterization of poly(vinylidene fluoride) composite membranes blended with nano-crystalline cellulose. Prog Nat Sci Mater Int 2012;22:250–7. https://doi.org/10.1016/j.pnsc.2012.04.011.

[48] Sinirlioglu D, Muftuoglu AE, Bozkurt A. Preparation of thin films from new azolic copolymers and investigation of their membrane properties. J Macromol Sci Part A Pure Appl Chem 2014;51:420–34. https://doi.org/10.1080/10601325.2014.893134.

[49] Shetty S, Mahendran A, Anandhan S. Development of a new flexible nanogenerator from electrospun nanofabric based on PVDF/talc nanosheet composites. Soft Matter 2020;16:5679–88. https://doi.org/10.1039/d0sm00341g.

[50] Duan Z, Jiang Y, Zhao Q, Huang Q, Wang S, Zhang Y, et al. Daily writing carbon ink: novel application on humidity sensor with wide detection range, low detection limit and high detection resolution. Sensor Actuator B Chem 2021;339:129884. https://doi.org/10.1016/j.snb.2021.129884.

[51] Zhu M, Shi Q, He T, Yi Z, Ma Y, Yang B, et al. Self-powered and self-functional cotton sock using piezoelectric and triboelectric hybrid mechanism for healthcare and sports monitoring. ACS Nano 2019. https://doi.org/10.1021/acsnano.8b08329.

[52] Nguyen V, Zhu R, Jenkins K, Yang R. Self-assembly of diphenylalanine peptide with controlled polarization for power generation. Nat Commun 2016;7:1–6. https://doi.org/10.1038/ncomms13566.

[53] Lee JH, Heo K, Schulz-Schönhagen K, Lee JH, Desai MS, Jin HE, et al. Diphenylalanine peptide nanotube energy harvesters. ACS Nano 2018;12:8138–44. https://doi.org/10.1021/acsnano.8b03118.